OPEN ACCESS



Probing Magnetic Fields in Protoplanetary Disk Atmospheres through Polarized Near-IR Light Scattered by Aligned Grains

Haifeng Yang (杨海峰)^{1,3} and Zhi-Yun Li²

¹ Kavli Institute for Astronomy and Astrophysics, Peking University, Yi He Yuan Lu 5, Haidian Qu, Beijing 100871, People's Republic of China hfyang@pku.edu.cn

² Department of Astronomy, University of Virginia, Charlottesville, VA 22903, USA Received 2022 March 7; revised 2022 July 6; accepted 2022 July 7; published 2022 August 15

Abstract

Magnetic fields play essential roles in protoplanetary disks. Magnetic fields in the disk atmosphere are of particular interest, as they are connected to the wind-launching mechanism. In this work, we study the polarization of the light scattered off of magnetically aligned grains in the disk atmosphere, focusing on the deviation of the polarization orientation from the canonical azimuthal direction, which may be detectable in near-IR polarimetry with instruments such as VLT/SPHERE. We show with a simple disk model that the polarization can even be oriented along the radial (rather than azimuthal) direction, especially in highly inclined disks with toroidally dominated magnetic fields. This polarization reversal is caused by the anisotropy in the polarizability of aligned grains and is thus a telltale sign of such grains. We show that the near-IR light is scattered mostly by μ m-sized grains or smaller at the $\tau=1$ surface and such grains can be magnetically aligned if they contain superparamagnetic inclusions. For comparison with observations, we generate synthetic maps of the ratios of U_{ϕ}/I and Q_{ϕ}/I , which can be used to infer the existence of (magnetically) aligned grains through a negative Q_{ϕ} (polarization reversal) and/or a significant level of U_{ϕ}/I . We show that two features observed in the existing data, an asymmetric distribution of U_{ϕ} with respect to the disk minor axis and a spatial distribution of U_{ϕ} that is predominantly positive or negative, are incompatible with scattering by spherical grains in an axisymmetric disk. They provide indirect evidence for scattering by aligned nonspherical grains.

Unified Astronomy Thesaurus concepts: Protoplanetary disks (1300); Magnetic fields (994); Polarimetry (1278)

1. Introduction

The evolution of protoplanetary disks is generally thought to be determined by magnetic fields through either magnetorotational instability (Balbus & Hawley 1991) or magnetized disk wind (Blandford & Payne 1982). The magnetic field structure in the disk atmosphere is of particular interest in understanding the wind-launching mechanisms. Strongly magnetized disks tend to launch magnetocentrifugal wind (MCW; Blandford & Payne 1982) with rigid and mostly poloidal magnetic field lines in the disk atmosphere. Weakly magnetized disks tend to launch magnetothermal disk winds (Bai et al. 2016) and rely on the vertical gradient of the magnetic pressure from the toroidal field to launch the wind. The magnetic field strength is also related to other interesting issues of protoplanetary disks, such as accretion rates.

Dust grains can trace the magnetic field if they are magnetically aligned (Andersson et al. 2015; Lazarian 2007). While polarized (sub)millimeter dust thermal emission has been proven to be a powerful tool to study magnetic fields on scales larger than the disks (e.g., Hull & Zhang 2019; Planck

Original content from this work may be used under the terms of the Creative Commons Attribution 4.0 licence. Any further distribution of this work must maintain attribution to the author(s) and the title of the work, journal citation and DOI.

Collaboration et al. 2020 and references therein), its application to the disk scale has not been as successful because we see mostly scattering-induced polarization at shorter (e.g., 870 μ m) wavelengths (Stephens et al. 2017; Bacciotti et al. 2018; Hull et al. 2018; Dent et al. 2019) and complicated nonmagneticorigin patterns at longer (e.g., 3 mm) wavelengths (Kataoka et al. 2017; Harrison et al. 2019). Yang (2021) showed that the Larmor precession in the disk midplane is likely too slow to ensure magnetic alignment, which is likely the reason behind the failure of polarized dust thermal emission to trace magnetic fields in disks. However, Yang (2021) proposed that the micron-sized dust grains in the disk atmosphere can potentially be magnetically aligned. This idea was partially supported by Li et al. (2016), who found polarized radiation at $10.3 \,\mu\text{m}$, which may be explained in part by thermal emission from grains aligned with the magnetic field in the disk atmosphere.

The Spectro-Polarimetric High-contrast Exoplanet REsearch (SPHERE) at the Very Large Telescope (VLT) has been used for high-resolution polarimetric observations of protoplanetary disks in scattered near-IR light (Benisty et al. 2015; Avenhaus et al. 2018; Garufi et al. 2020, 2022). These studies usually focus on the azimuthal Stokes parameter Q_ϕ component to produce high-resolution images of protoplanetary disks. The U_{ϕ} component is often observed to be small and its divergence from zero is a sign of deviation from the simplest single Rayleigh scattering. Theoretically, Canovas et al. (2015) used a generic transition disk model with large dust grains to show that the scattered light from moderately inclined disks can possess a significant U_{ϕ} . Whitney & Wolff (2002) studied the scattering by aligned grains but focused on the circular polarization in the protostellar envelope. Our focus in this paper is on the near-IR photons scattered by aligned dust grains

³ Boya Fellow

⁴ In the context of disk dynamics, the disk atmosphere is often defined as where the disk winds are launched. In the context of near-IR scattering polarimetry, the disk atmosphere is the optical depth of unity surface. Both locations are a few gas scale heights above the disk midplane, and we use "disk atmosphere" to denote both, even though they are not strictly at the same location.

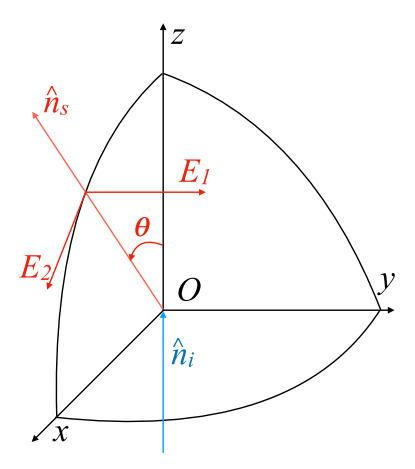


Figure 1. The geometry of a simple setting in the grain frame. The photon propagating in the \hat{z} direction is scattered by the dust grain sitting at the origin O toward the \hat{n}_s direction in the xOz plane. The scattering angle is θ . The scattered light is decomposed into E_1 and E_2 directions. Note that it is often assumed that the scattered light is polarized along E_1 direction.

in the atmosphere of protoplanetary disks, which can potentially have polarization patterns different from the commonly expected pure azimuthal ones.

The structure of the paper is as follows. In Section 2 and Appendix A, we discuss the polarization of scattered light in the grain frame, focusing on the difference with spherical dust grains. In Section 3, we calculate the polarization pattern in a disk configuration. In Section 4, we discuss the grain size distribution and grain alignment at the optical depth $\tau=1$ surface in a generic protoplanetary disk model. In Section 5, we discuss our results, including the detectability of the U_{ϕ} produced by the scattering of magnetically aligned grains, the differences between the patterns produced by aligned grains and multiple scattering of spherical grains, and implications for observations. We summarize our results in Section 6.

2. Basic Physics

Before considering the general case in a disk environment. we first illustrate the basic physics of why the polarization orientation of the light scattered by aligned grains can be different from that by spherical grains in a simple setup in the grain frame. We consider a Cartesian coordinate system xyz (see Figure 1). Let \hat{z} be the propagation direction for incoming light. Without loss of generality, we fix the scattered light in the xOz plane, with O being the particle location. Let θ be the scattering angle, the scattering directional vector is then $(\sin \theta, 0, \cos \theta)$. Since light is a transverse wave, its E vector can be decomposed into two components that are perpendicular to the scattering direction. We call the component perpendicular to both incoming and scattering lights E_1 (in the \hat{e}_1 direction), and the other component E_2 (in the \hat{e}_2 direction). We can easily see that the E_1 direction is also the \hat{y} direction of our coordinate system. If the dust particle is spherical, the scattered light can either be polarized along E_1 or along E_2 direction, due to the symmetry of this scattering geometry. If we define the Stokes parameters such that fully polarized light with polarization along E_1 has Q = I, the Stokes U is always zero for spherical dust grains. If the dust particle is not spherical, and if \hat{x} and \hat{y} are not the principal axes of the dust particle, the light will no longer be polarized along either E_1 or E_2 direction, which leads to a nonzero Stokes U component. The break of the symmetry is the reason why the polarization can deviate from the spherical case.

It turns out that the deviation is always maximized in the forward and backward scattering directions. For the forward scattering, we have the scattering direction being the same as the incoming light direction (\hat{z}) . If the dust particle is spherical, the scattered light will always be nonpolarized, because of the symmetry. If the dust particle is nonspherical, say being elongated along \hat{x} direction, then the scattered light would be polarized along the \hat{x} direction, which is qualitatively different from the spherical case. If we change the scattered light slightly away from the forward scattering direction with a small scattering angle θ in the xOz plane, then the light scattered by a spherical dust grain would be polarized along \hat{y} direction, in the often assumed Rayleigh scattering regime. For dust grains elongated along \hat{x} direction, on the contrary, this small deviation in scattering angle is not enough to change the polarization state of the scattered light, and the scattered light is still polarized along \hat{x} direction. Hence the angle difference between the polarization orientation of light scattered by spherical dust grains and the polarization orientation of light scattered by elongated dust grains near the forward scattering direction can always be as large as 90°, as they are perpendicular to each other in the setup we discussed above.

In Appendix A, we discuss the angle difference in the grain frame in more detail. We show that the angle difference between the spherical dust grain and the elongated dust grain can easily reach 10° in the grain frame. We also show that the angle difference increases with the angle between the symmetry axis of the dust particle and the incoming light direction and with the aspect ratio of the dust particle. It also depends on the compositions of the dust grains. In what follows, we focus on the angle difference in a disk environment where most of the relevant observations are carried out.

3. Polarization in the Disk Atmosphere

3.1. Model Prescription

Calculations in Section 2 and Appendix A focus on the polarization of the scattered light in the grain frame. While more physically intuitive, it is not directly connected to the observed polarization. Here we study the scattered light in a protoplanetary disk, focusing on the deviation of polarization orientation from the direction perpendicular to the stellar light, and the expected polarization orientation in the small spherical particle regime.

To calculate the polarization orientation in the scattered light from the surface of a protoplanetary disk, we consider a setup shown in Figure 2. The black horizontal arrow represents the disk midplane. The red dot represents the dust particle that scatters light from \hat{n}_1 direction toward the \hat{n}_2 direction, which makes an angle i with the z direction, the direction perpendicular to the disk midplane; i is simply the disk inclination angle (i = 0 is face-on). Note that only one dust grain is plotted in the figure, but it represents a ring of dust grains, all of which have the same cylindrical radius R from the star and height H above the disk midplane. We assume that the local magnetic field \boldsymbol{B} makes an angle θ_B with the z direction, and an azimuthal angle ϕ_B from the x direction, such that $\phi_B = 0$ implies a pure poloidal magnetic field. As usual, we assume that the grains are aligned with their shortest axis along the magnetic field direction. If the grains are spinning around

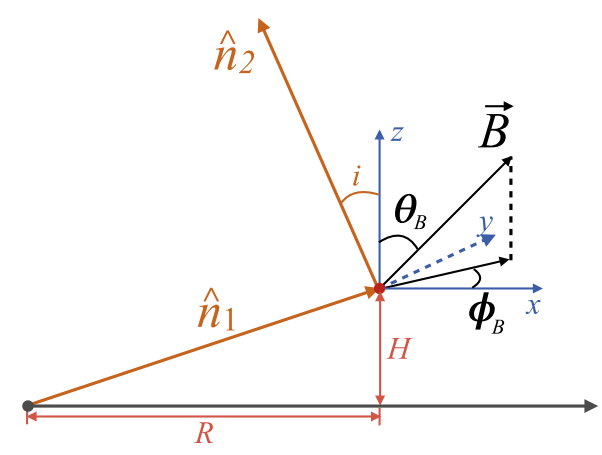


Figure 2. The geometry of our setup in the disk frame. The black dot represents the central star. The red dot represents the scattering dust grain. Hence \hat{n}_1 connecting these two dots is the incoming light direction. The scattered light propagates along \hat{n}_2 , making an angle of i with the z-axis. The local magnetic field direction is prescribed by the angles θ_B and ϕ_B . See text for more details.

the B field, they would be effectively oblate after assemble-averaging independent of their intrinsic shapes.

We adopt the same dust composition as used in Appendix A, which is the same as the one adopted by Birnstiel et al. (2018), and assume the dipole approximation for simplicity. We consider five parameters: H/R, i, θ_B , ϕ_B , and the dust aspect ratio s.

3.2. A Limiting Sase: Purely Toroidal Magnetic Field

Before studying the polarization pattern in a generic model, we will first consider a limiting case that will help our understanding: a purely toroidal magnetic field along \hat{y} direction, with $\theta_B=90^\circ$ and $\phi_B=90^\circ$. The incoming light propagating along \hat{n}_1 direction can be decomposed along two directions: \hat{y} and $\hat{n}_1 \times \hat{y}$. We will denote the dipoles excited by these two components P_1 and P_2 , respectively. See Figure 3 for a schematic illustration of this setting.

The angle between the scattered light direction \hat{n}_2 and the P_2 , defined as ι , will be important to our analysis that follows. Note that in the disk frame, we have $\iota = i + (-)\tan^{-1}(H/R)$ for the near (far) side of the ring considered in Figure 2.

Because the dust grains are aligned with the magnetic field in P_1 direction, we have $P_1 = \alpha_3 E_1$. Since P_1 is always perpendicular to \hat{n}_2 , we have $E_{s1} \propto P_1 \propto \alpha_3$, where $E_{s1,2}$ is the E vector of scattered light induced by $P_{1,2}$. Similarly, we have $P_2 = \alpha_1 E_2$. Since P_2 is making an angle ι with \hat{n}_2 , we have $E_{s2} \propto P_2 \sin \iota \propto \alpha_1 \sin \iota$. If $E_{s1} > E_{s2}$, the scattered light is polarized along E_{s1} direction, i.e., the direction perpendicular to both \hat{n}_1 and \hat{n}_2 , which is the canonical (azimuthal) polarization direction for spherical particles. If $E_{s1} < E_{s2}$, the scattered light is polarized along E_{s2} direction, i.e., the P_2 projected toward the sky plane, the plane perpendicular to \hat{n}_2 . This is also the direction of the projected \hat{n}_1 (radial) direction and is perpendicular to the canonical polarization direction for spherical particles. The polarization direction is changed by 90° and the Q_{ϕ} , the azimuthal Q parameter (de Boer et al. 2020), changes from positive to negative. We call this "polarization reversal". Define the critical angle ι_c as $\iota_c \equiv \sin^{-1}(|\alpha_3|/|\alpha_1|)$. For $\iota > \iota_c$ ($\iota < \iota_c$), we have $E_{s2} > E_{s1}$ ($E_{s2} < E_{s1}$), and the polarization is (not) reversed. The dependence of the critical angle with a dust aspect ratio is shown in Figure 4.

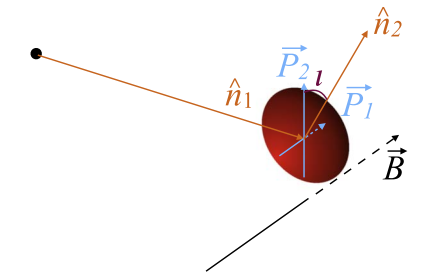


Figure 3. The geometry of an oblate grain aligned by a pure toroidal magnetic field. By definition, the magnetic field \boldsymbol{B} is perpendicular to the incoming light direction \hat{n}_1 . The incoming light excites two dipoles in the grain, denoted as \boldsymbol{P}_1 and \boldsymbol{P}_2 . The scattered light direction \hat{n}_2 makes an angle of ι with \boldsymbol{P}_2 . Note that we have $|\boldsymbol{P}_2| > |\boldsymbol{P}_1|$ under this configuration.

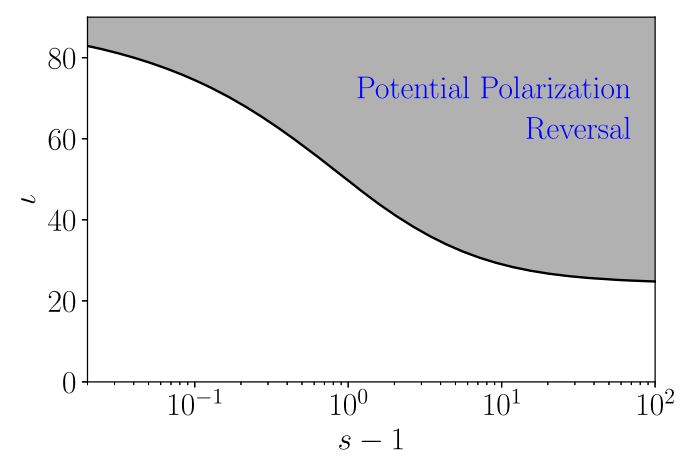


Figure 4. The critical curve for polarization reversal. The s in the x-axis is the aspect ratio of dust grains. The ι is the angle between the scattered light propagating direction \hat{n}_2 and the second dipole direction P_2 (see, Figure 3). In the gray parameter space, the polarization is potentially reversed, i.e., the light is polarized along that radial, rather than the canonical azimuthal direction.

In Section 3.3, we discuss a fiducial case of a moderately inclined disk with $\iota > \iota_c$ but not a purely toroidal magnetic field. We will demonstrate that the polarization reversal still exists (i.e., it is not limited to the pure toroidal magnetic field configuration) and is likely once we reach the critical angle. In Section 3.4, we present a less inclined disk model without polarization reversal. We will show that there is still an appreciable angle deviation from the azimuthal pattern that is potentially detectable with VLT/SPHERE.

3.3. Fiducial Case

For the fiducial case, we consider H/R = 0.2, $i = 60^{\circ}$, s = 1.5, $\theta_B = 45^{\circ}$, and $\phi_B = 90^{\circ}$ (Model 1 hereafter). The last two angles imply that the toroidal to poloidal magnetic field ratio is $B_{\rm tor}/B_{\rm pol} = 1$. We can easily calculate the ι at the near side as $\iota = i + \tan^{-1}(H/R) = 71^{\circ} > \iota_c = 59^{\circ}$. The results are shown in Figure 5. In the left panel, we show the polarization orientation at each location on a dust ring of constant cylindrical radius R and height H in the sky plane, with black unilength line segments. To guide the eyes, we also use dotted lines to connect the central star and the scattering grains. In the often assumed case, the polarization is perpendicular to the dotted line, shown as red lines, with only the Q_{ϕ} component being nonzero. We can see that the polarization is completely reversed near an azimuthal angle of 330°. To show the deviation more quantitatively, we plot the angle difference as a

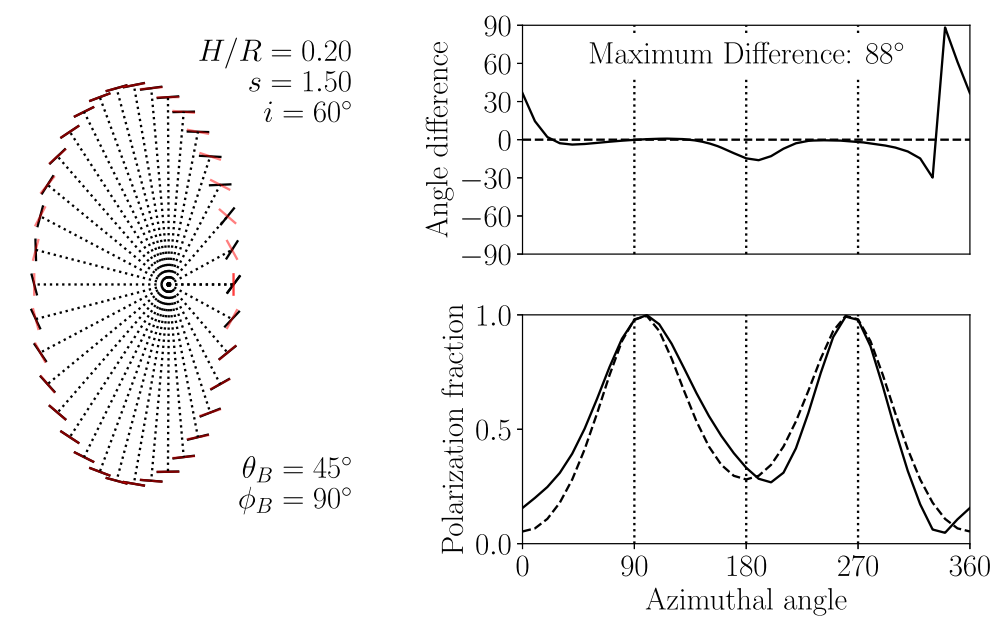


Figure 5. The polarization pattern in our fiducial disk model (Model 1). The parameters adopted are listed in the left panel. See Figure 2 for their definitions. Left: the black unilength line segments represent the polarization orientation. The dotted lines connect the central star with each test scattering grain. The red line segments are perpendicular to the dotted lines and represent the often assumed azimuthal polarization patterns. Upper right: the difference in polarization orientation as a function of the azimuthal angle of the test scattering grain in the disk frame. The polarization is essentially "reversed" and is along the radial direction at an azimuthal angle of 330°. Lower right: the polarization fraction as a function of the azimuthal angle. The solid line represents the fiducial case, whereas the dashed line represents the small spherical grain case.

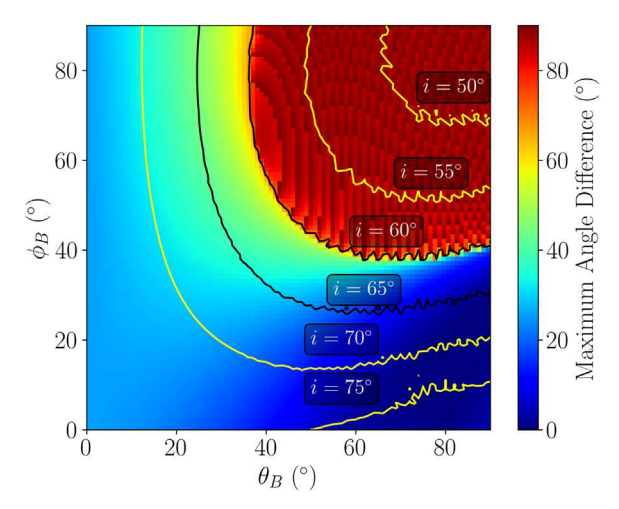


Figure 6. The maximum angle difference for different configurations of magnetic fields, assuming an inclination angle of 60° , H/R of 0.2, and a dust aspect ratio of s=1.5. The color map represents the maximum angle difference $\Delta\eta$. Also plotted are contours of constant angle difference $\Delta\eta=70^{\circ}$ for different inclination angles. The inclination angle i is labeled next to each line.

function of the azimuthal angle (of dust grains in the disk frame) in the upper right panel. The polarization fraction, the ratio $p \equiv \text{PI/I}$ between the polarized intensity and the total intensity, as a function of the azimuthal angle, is shown in the lower right panel as a solid line. The polarization fraction for scattering by small spherical grains is also shown as a dashed line. We can see that the polarization is still maximized at 100%, while the phase function deviates from the spherical curve slightly. We can see that the polarization reversal location coincides with low polarization points because it relies on the usually subdominant component P_2 to overwhelm the P_1 to have polarization reversal (see Section 3.2).

The same calculation is repeated on a finer azimuthal grid (360 points to sample the full azimuthal extent) with different combinations of the angles θ_B and ϕ_B that specify the magnetic field configurations. The maximum angle difference for each combination is shown as a color map in Figure 6, with θ_B and ϕ_B as the x- and y-axis, respectively. We can see that the ϕ_B has a very strong effect on the angle difference. In the upper right part of Figure 6, the maximum angle difference is essentially 90° (i.e., polarization reversal). The fluctuations are due to the finite resolution of the azimuthal grid, and we have tested that the fluctuations become smaller (with the angle deviation closer to 90°) with an increasing number of grid points. Away from the upper right polarization reversal region, the angle difference is still appreciable, and can easily be above 20° for our fiducial disk inclination of 60°.

To study the dependence of the polarization reversal region on the observing inclination angle i, we first find for the fiducial $i=60^\circ$ all pairs of θ_B and ϕ_B that would make the angle difference $\Delta \eta = 70^\circ$. The resulting constant angle difference $\Delta \eta = 70^\circ$ contour is labeled in Figure 6. We then repeat the same calculation for several inclination angles. The resulting contours are labeled in the figure as well. We can see that the parameter space with polarization reversal as marked by the $\Delta \eta = 70^\circ$ contour increases with increasing inclination angle. In the most inclined case, the polarization reversal is almost inevitable, with only a small region in the lower right corner being not completely reversed (the maximum angle difference is still large). We would like to note that highly inclined disks are also subject to strong forward scattering and potentially multiple scattering (Canovas et al. 2015). These effects, not

⁵ The choice of $\Delta \eta = 70^{\circ}$ is somewhat arbitrary. Because of the steep gradient toward the polarization reversal region, other choices between $\sim 70^{\circ}$ and $\sim 85^{\circ}$ have little effect on the contours except for the one for the most inclined ($i = 75^{\circ}$) case. We choose 70° to minimize the wiggles on the $i = 75^{\circ}$ curve.

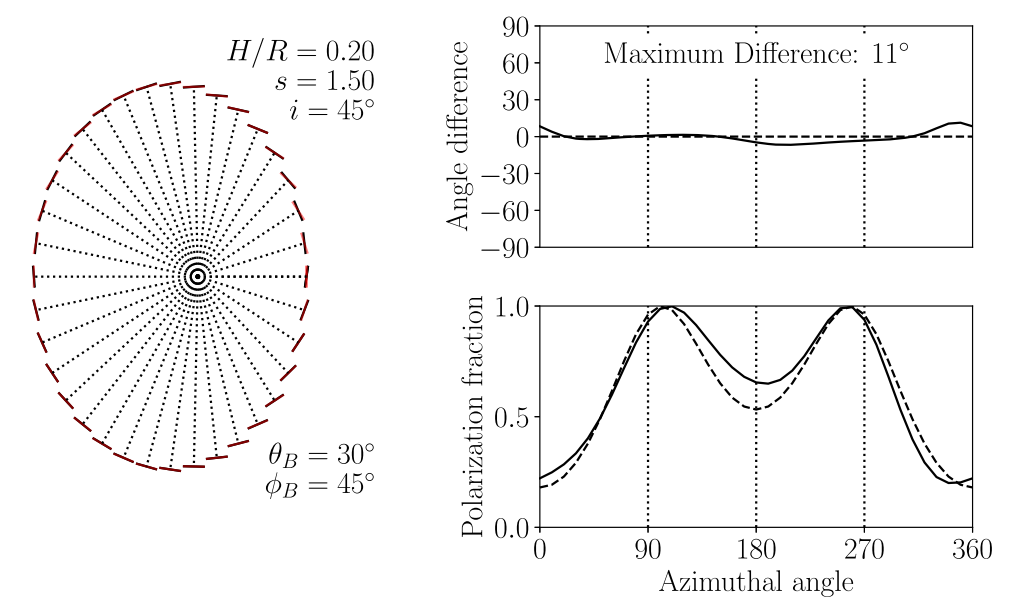


Figure 7. The same as Figure 5, but for Model 2. This represents a less inclined disk model with a moderate magnetic field configuration. There is no polarization reversal. The maximum angle difference is only 11° but still detectable at the 3σ level if S/N > 7.8 for the Stokes parameters.

considered in this simple first study, may change the results substantially.

3.4. Less Inclined Case

We have shown that for highly inclined disks, the polarization can be reversed, with an orientation along the radial, rather than the canonical azimuthal, direction. We now focus on less inclined cases, particularly the dependence of the maximum angle difference with the observing inclination angle i in the disk frame.

As an example of a smaller inclination angle, we assume H/R=0.2, s=1.5, and $i=45^\circ$. We also assume a less extreme configuration for the magnetic field with $\theta_B=30^\circ$ and $\phi_B=45^\circ$. The results for this model (Model 2 hereafter) are shown in Figure 7. We can see that for this less inclined disk model, the maximum angle difference is 11°. Note that the toroidal to poloidal magnetic field ratio is $B_{\rm tor}/B_{\rm pol}=1/\sqrt{7}\approx 0.38$. In Section 5.1, we derive a rough error estimate formula for the angle deviation as $\delta\eta\approx 1/(2({\rm S/N}))$, with S/N being the signal-to-noise ratio. The angle difference of 11° can be detected at a signal-to-noise level of $\delta\eta/\Delta\eta=0.38$ S/N. If we ask for 3σ detection for the angle difference, we need only an S/N of 7.8, easily achievable with VLT/SPHERE.

If we allow the magnetic field configuration to change while fixing the other parameters, we get the maximum angle difference in the (θ_B, ϕ_B) map shown in Figure 8. We can see that the trend is similar to our fiducial model, except that there is no polarization reversal in this map. The maximum angle difference increases as we increase the ϕ_B . Even for this moderate inclination angle of $i = 45^{\circ}$, as ϕ_B approaches 90°, the angle difference can easily reach 20° or even 30°. The azimuthal angle of the magnetic field, ϕ_B , also determines the ratio of the toroidal component to the poloidal component of the magnetic field, which is very important in determining the wind-launching mechanisms. Disks with large magnetization have rigid magnetic field lines and tend to launch magnetocentrifugal winds with a small toroidal component. Weakly magnetized disk, on the other hand, will have magnetic field lines winded up into a mostly toroidal configuration first. The

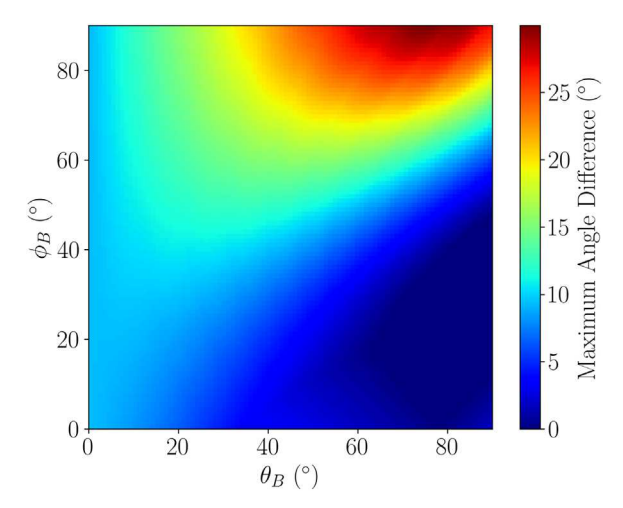


Figure 8. The same as Figure 6 but for $i = 45^{\circ}$, H/R = 0.2, s = 1.5, and without the constant angle difference $\Delta \eta = 70^{\circ}$ contours. Note the difference in the color map.

disk wind is then launched due to a vertical gradient of magnetic pressure (Bai et al. 2016).

The maximum angle differences in the (θ_B, ϕ_B) map can be calculated for different inclination angles i while fixing H/R=0.2. The results for three different dust aspect ratios s=0.1, 1.5, and 2.0 are shown in Figure 9. We can see that the behaviors are similar among different s: the maximum angle difference gradually increases before reaching about 30° , then it suddenly jumps to 90° and enters the polarization reversal regime, the gray region in Figure 4. So for disks with small inclination angles, say $i < 20^\circ$, the deviation from the azimuthal polarization pattern due to grain alignment is likely negligible.

4. Analysis in a Disk Model

4.1. Disk Model Adopted

In this section, we perform a simple analysis of scattering in the disk atmosphere problem. To do so, we adopt a Minimum

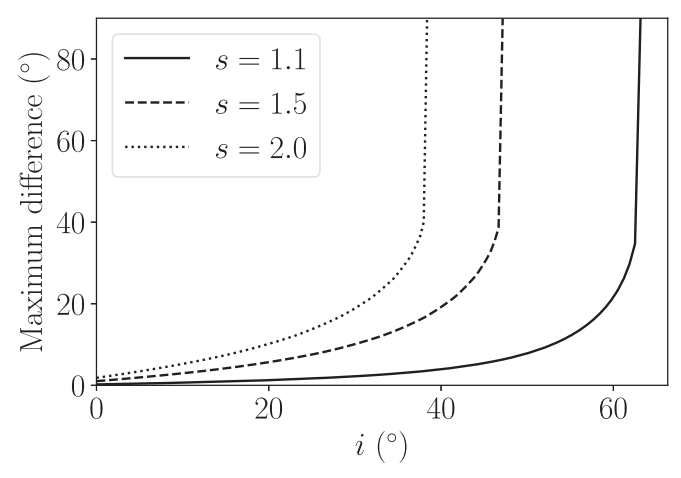


Figure 9. Maximum angle difference as a function of inclination angle i, for H/R = 0.2 and three different dust aspect ratios s = 1.1, 1.5, and 2.0.

Mass Solar Nebular model (Weidenschilling 1977) with a column density $\Sigma(R) = \Sigma_0 R_{\rm au}^{-1.5}$, where $\Sigma_0 = 10^3 \, {\rm g \ cm^{-2}}$ and $R_{\rm au}$ is the cylindrical radius in units of au. We assume a vertically isothermal temperature profile with $T(R) = T_0 \ R_{\rm au}^{-0.5}$, with $T_0 = 300 \, {\rm K}$. This results in a mildly flared disk with $(H_g/R) = 0.045 \ R_{\rm au}^{1/4}$, where H_g is the gas scale height. The dust scale height is different from H_g and depends on the grain size, as (Youdin & Lithwick 2007):

$$H_d(R, a) = H_g(R) \left(1 + \frac{\text{St}}{\alpha} \frac{1 + 2\text{St}}{1 + \text{St}} \right)^{-1/2},$$
 (1)

where $St = \rho_s a/\Sigma$ is the Stokes number that determines how well the dust grains are coupled with the gas, and α is the turbulence parameter, which we take to be $\alpha = 10^{-4}$. We assume dust grains have a power-law distribution (Mathis et al. 1977): $N(a) \propto a^{-3.5}$ after vertical integration, between $a_{min} = 0.01 \,\mu$ m and $a_{max} = 1$ mm. The total column density of the dust grains is 0.01Σ , where a gas-to-dust ratio of 100 is assumed. In practice, we use 100 bins of dust grains distributed evenly in logarithmic space, each represented by the center of the bin. For each bin, the dust grains follow vertical Gaussian distributions according to a scale height from Equation (1).

4.2. Grain Size at $\tau = 1$ Surface

The $\tau=1$ surface is the surface where radial optical depth τ reaches 1. This is where the stellar light is scattered by the dust grains, and the properties of dust grains at this surface are very important.

In order to calculate the $\tau=1$ surface, we calculate the extinction cross section at 1.5 μm for grains of different sizes using Mie theory (Bohren & Huffman 1983) through the miepython module. We then integrate the optical depth at $\lambda=1.5~\mu m$ radially outward from the center of the disk. The $\tau=1$ contour is shown in the upper panel of Figure 10. Also shown in the upper panel as a dashed line is the H/R of the surface. We can see that the $\tau=1$ surface is largely flat, despite the fact that our disk model is mildly flared. There are two reasons for this flat surface. On the one hand, the dust settles toward the midplane more at large radii due to the less turbulent stirring from the more diffuse gas. This effect can also be

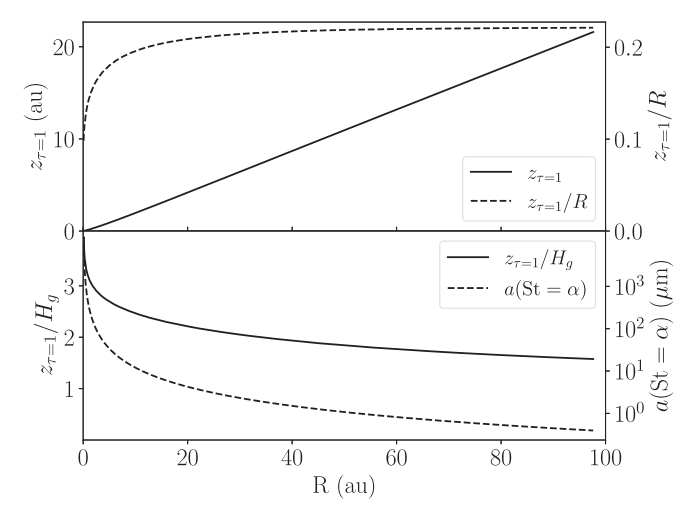


Figure 10. The $\tau=1$ surface. Top: the solid line represents the height of $\tau=1$ surface as a function of radius, whereas the dashed line shows the H/R of this surface. Bottom: the solid line shows the height of $\tau=1$ surface in terms of local gas scale height. The dashed line represents the critical grain size as a function of radius defined by setting the Stokes number equal to the viscous parameter α .

viewed in the lower panel of Figure 10, where the $z_{\tau=1}/H_g$ is plotted against R as a solid line. We can see that the $\tau=1$ surface in terms of the gas scale height H_g gradually decreases. On the other hand, and probably more importantly, the outer regions are blocked or "shadowed" by the inner regions, so that the $\tau=1$ surface can never bend toward the midplane.

Note that Avenhaus et al. (2018) find that the protoplanetary disks are moderately flared, as opposed to being flat in our model. In our turbulent stirring model, if we fix the grain size, the Stokes number goes as St $\sim R^{\gamma}$, where $-\gamma = -1.5$ is the power-law index for the adopted column density profile. In the limit of $\alpha \ll \text{St} \ll 1$, we have $H_d/H_g \sim \text{St}^{-1/2} \sim R^{-\gamma/2}$. The gas scale height is $H_g/R \sim R^{(1-q)/2}$, with -q = -0.5 being the power-law index for the temperature profile. So we have, for fixing grain size a, $H_d/R \sim R^{(1/2)(1-q-\gamma)}$. Since we have adopted q = 0.5, $\gamma = 1.5$, the $H_{\rm d}/R$ decreases with R, and the dust at larger radii is shadowed by the dust at inner radii. If we require the near-IR scattering surface to be flared as well, we need $q + \gamma < 1$. This is very hard to achieve. The requirement may be alleviated with the introduction of radial variation of turbulent α . If α goes as R^{ω} , i.e., the disk is more turbulent at a larger radius, the above constraint becomes $q + \gamma < 1 + \omega$. Another potential and more likely way to make a flaring scattering surface is to abandon the turbulent stirring model and introduce a disk wind, which may entrain small grains and make the disk appear flaring. We will not discuss these alternatives in more detail in what follows. The turbulent stirring model we introduce here is only for illustrative purposes and to lay the foundations for the following discussions on synthetic maps and grain alignments, both of which are not sensitive to whether the disk is flared or not.

In the lower panel of Figure 10, we also plot the grain size with $St = \alpha$ as a function of R. It characterizes the maximum size of the grains that can be stirred up to a height comparable to the gas scale height (see, Equation (1)).

To view the dust distribution at $\tau=1$ surface more clearly, we plot the mass, number density, and extinction cross section at R=30 au for each grain size bin in Figure 11. The mass ΔM is the mass density of dust grains between a and $a+\Delta a$. The

⁶ Credit: Scott Prahl. Available at https://github.com/scottprahl/miepython.

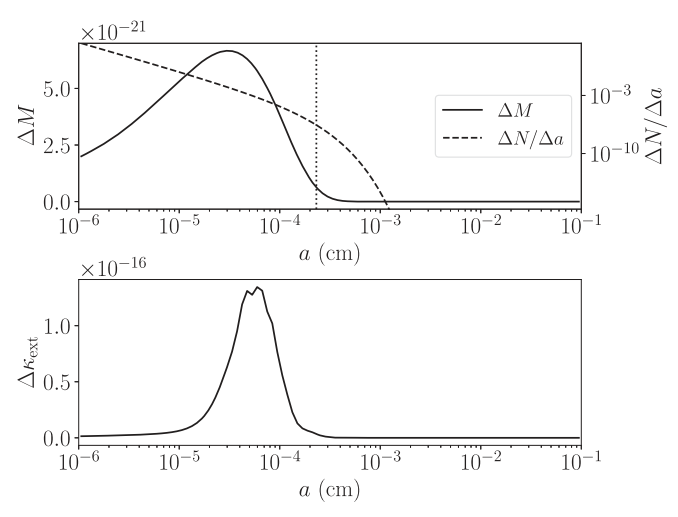


Figure 11. The mass, number density, and extinction opacity as a function of different grain sizes at the $\tau=1$ surface of R=30 au.

number density is $\Delta N/\Delta a = \Delta M/(m_a \Delta a)$, with $m_a = \rho_s(4\pi/3)a^3$ being the mass of a grain with radius a. The extinction cross section is defined as $\Delta \sigma_{\rm ext} = \Delta M \kappa_{\rm ext}(a)$, with $\kappa_{\rm ext}(a)$ being the extinction opacity for the grains of radius a.

At R=30 au, we have $z_{\tau=1}=6.4$ au, and $a({\rm St}=\alpha)=2.3\,\mu{\rm m}$. When the grain size increases beyond 1 $\mu{\rm m}$, the mass and the number density drop very quickly. The extinction is also dominated by grains with a radius of $\sim\!0.6\,\mu{\rm m}$, or a size parameter of $2\pi a/\lambda\sim2.5$. This justifies our discussion on grain size in Appendix A.6 and the adoption of dipole approximation in most of this work.

4.3. Synthetic Maps

With the $\tau=1$ surface and the corresponding H/R obtained, we can calculate the Stokes parameters at each location and generate synthetic maps. In order to focus on the deviation from the azimuthal pattern, we choose to show maps of the ratios of azimuthal Stokes parameters, U_{ϕ}/I and Q_{ϕ}/I . The results for Model 1 and Model 2 are shown in Figure 12. In order to make small values more visible while using the same color map for all panels, we adopt symmetric logarithmic normalization with a linear scale between -0.1 and 0.1.

For Model 1, we have polarization reversal (polarization in the radial direction), which manifests itself as a negative wedge in the Q_{ϕ}/I map. The magnitude of the negative wedge is small (\sim 0.05) because the polarization reversal coincides with low polarization points. The U_{ϕ}/I in Model 1 can be as large as \sim 0.15, and can be both positive and negative.

For Model 2, we do not have polarization reversal so that all Q_{ϕ}/I are positive. The magnitude of U_{ϕ}/I is also smaller compared to the more inclined Model 1 and stays below ~ 0.05 over most of the disk.

Last but not the least, the sign of U_{ϕ} depends on the direction of the toroidal magnetic field. If we change the ϕ_B to $-\phi_B$, the Q_{ϕ}/I maps are unaffected but the U_{ϕ}/I maps will change signs everywhere while keeping the magnitude the same. This behavior, alongside information on disk rotation directions, can be used to distinguish it from other mechanisms that produce U_{ϕ} , such as through multiple scattering (Canovas et al. 2015). We will discuss how to distinguish our U_{ϕ} -producing mechanism from others in more detail in Section 5.2.

4.4. Grain Alignment at $\tau = 1$ Surface

In this section, we briefly discuss the grain alignment at the $\tau=1$ surface based on the timescales of several most relevant processes. The discussion is similar to Tazaki et al. (2017) and Yang (2021).

1. The gaseous damping timescale: it determines how fast random collisions with gas particles disalign dust grains and is given by:

$$t_{\rm d} = 7.1 \times 10^5 \,\mathrm{s} \times \left(\frac{\rho_{\rm s}}{3 \,\mathrm{g \, cm}^{-3}}\right) \times \left(\frac{a}{1 \,\mu\mathrm{m}}\right) \left(\frac{n_{\rm g}}{10^9 \,\mathrm{cm}^{-3}}\right)^{-1} \left(\frac{T_{\rm g}}{85 \,\mathrm{K}}\right)^{-1/2},$$
 (2)

where ρ_s is the solid density of dust grains, n_g is the number density of gas molecules (assuming a mean molecular weight of 2.3). For our adopted disk model at $\tau = 1$ surface and 1 μ m dust grains, the gaseous damping timescale is plotted as a blue curve in Figure 13.

2. The Larmor precession timescale: it is the timescale that rotating dust grains with magnetic moment due to the Barnett effect (Barnett 1915) precess around an external magnetic field:

$$t_L = 1.5 \times 10^6 \,\mathrm{s} \times \hat{\chi}^{-1} \hat{\rho}_s \left(\frac{T_d}{85 \,\mathrm{K}} \right) \times \left(\frac{B}{5 \,\mathrm{mG}} \right)^{-1} \left(\frac{a}{1 \,\mu\mathrm{m}} \right)^2, \tag{3}$$

where T_d is the dust temperature which we take to be the same as the midplane gas temperature prescribed above (vertically isothermal). For the magnetic field, following Yang (2021), we adopt the estimate from Bai (2011):

$$B = 1.0 \text{ G} \times \left(\frac{\dot{M}}{10^{-8} \text{ M}_{\odot} \text{ yr}^{-1}}\right)^{1/2} \left(\frac{r}{1 \text{ au}}\right)^{-11/8}, \tag{4}$$

where we have assumed the mass accretion rate $\dot{M} = 10^{-8} M_{\odot} \text{ yr}^{-1}$, typical for classical T Tauri stars (Hartmann et al. 2016).

The Larmor precession timescale is plotted as an orange curve in Figure 13. It is possible for dust grains to carry superparamagnetic inclusions (Jones & Spitzer 1967), which can shorten the Larmor precession timescale by up to a factor of $\hat{\chi} \sim 10^3$ (Yang 2021). We also plot the Larmor precession timescale with superparamagnetic inclusions with $\hat{\chi}=10^3$ as a green curve.

3. Radiative alignment torque (RAT) precession timescale: it is the timescale for the precession due to the radiative alignment torque (Lazarian & Hoang 2007). It can be estimated as (Tazaki et al. 2017):

$$t_{\text{rad,p}} = 8.8 \times 10^{4} \,\text{s} \times \hat{\rho}_{s}^{1/2} \hat{s}^{-1/3} \left(\frac{a}{1 \,\mu\text{m}}\right)^{1/2} \left(\frac{T_{d}}{85K}\right)^{1/2} \times \left(\frac{u_{\text{rad}}}{10^{6} \,u_{\text{ISRF}}}\right)^{-1} \left(\frac{\bar{\lambda}}{0.89 \,\mu\text{m}}\right)^{-1} \left(\frac{\gamma \,|\overline{Q}_{\Gamma}|}{0.4}\right)^{-1}, \tag{5}$$

where $\bar{\lambda}$ is the energy weighted averaged wavelength of the radiation, γ is the anisotropy of the radiation, and $u_{\rm ISRF} = 8.64 \times 10^{-13}$ is the interstellar radiation energy density (Mathis et al. 1983). We consider only the stellar light, hence $\gamma = 1$.

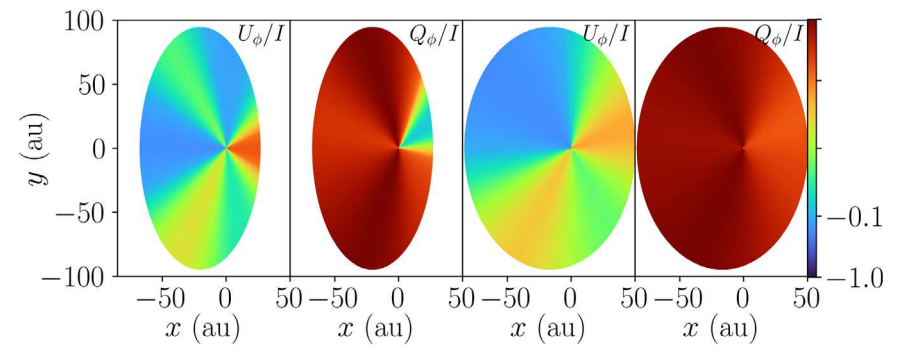


Figure 12. Synthetic maps. The left two panels are U_{ϕ}/I and Q_{ϕ}/I for Model 1 with $i=60^{\circ}$. The right two panels are the same, but for Model 2 with $i=45^{\circ}$. Note that the color map is the same for all panels and uses symmetric logarithmic normalization while being linear between -0.1 and 0.1.

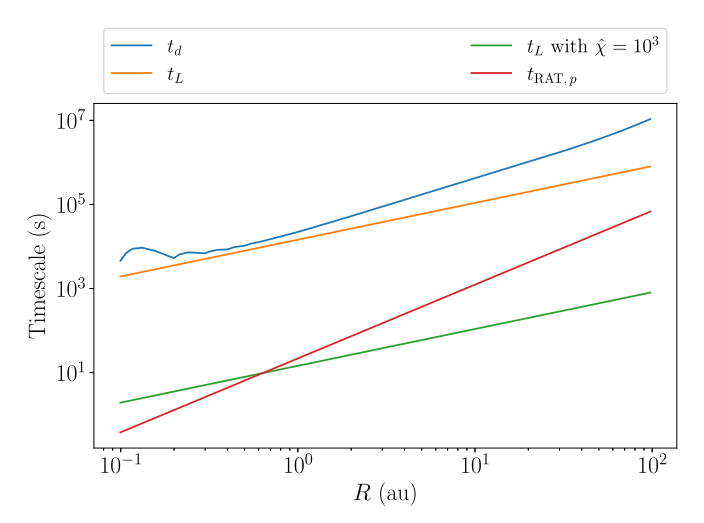


Figure 13. Timescale comparisons for grain alignment.

For radiation energy density $u_{\rm rad}$, we assume solar parameters, with an effective temperature of ~ 6000 K and bolometric luminosity $L = L_{\odot}$. This yields:

$$u_{\rm rad} = \frac{L}{4\pi R^2 c} = 4.564 \times 10^{-5} R_{\rm au}^{-2} \,\mathrm{erg} \,\mathrm{cm}^{-3},$$
 (6)

and $\bar{\lambda}=0.89\mu m$. Since $\bar{\lambda}\leqslant 1.8a$, we have $|Q_{\Gamma}|\approx 0.4$ (Lazarian & Hoang 2007). The RAT precession timescale is plotted as a red curve in Figure 13.

From Figure 13, we can see that $t_{RAT,p}$ is always smaller than t_d , indicating efficient radiative alignment torque. If the dust grains are of regular paramagnetic materials (orange curve), we also have $t_L > t_{RAT,p}$. In this case, we have k-RAT, i.e., grains aligned with radiation flux. As a result, the dust grains are aligned with short axes along the stellar light direction. As a result, the dust grains would look round from the star, and they scatter stellar light exactly the same as spherical dust grains in the dipole regime with small particles. Hence we expect no deviation from the azimuthal pattern if dust grains are aligned with k-RAT.

If the dust grains possess superparamagnetic inclusions (SPIs), the Larmor precession timescales can be reduced by a factor up to about 10^3 (Yang 2021). In this case (the green curve), we have $t_L > t_{\rm RAT,p}$ outside a radius of 0.7 au. So it is likely that superparamagnetic dust grains are aligned with the magnetic field rather than the radiation flux for the majority of the disk at tens of au scale. As SPI candidates are seen in meteorites (Goodman & Whittet 1995), it is possible that dust

grains in the disk atmosphere possess SPIs as well. The near-IR wavelength scattering polarimetry of protoplanetary disks can be an excellent probe for the existence of SPIs, which will help understand the magnetic alignment of large dust grains in other environments.

Lastly, it is worth mentioning that internal relaxation can also be problematic in disk atmosphere. Tazaki et al. (2017) estimated the internal relaxation timescale as a function of grain radius in their Figure 2 and showed that the internal relaxation timescale of 1 μ m dust grains can be tens of years, longer than any of the timescales considered in Figure 13. In this case, the degree of alignment may be reduced due to the lack of internal relaxation (Hoang & Lazarian 2009; Tazaki et al. 2017). More detailed and quantitative discussion and modeling on grain alignment is beyond the scope of this paper and will be deferred to future investigations.

5. Discussion

5.1. Detectability

In previous sections, we have shown that the angle deviation from azimuthal polarization can easily reach 10° or more for a moderately inclined disk. Here we discuss the detectability of such angle deviations.

The angle with azimuthal direction can be calculated through $\eta=(1/2)\arctan 2(U_\phi,\,Q_\phi)$. Without loss of generality, we limit our discussion here to the quadrant where $Q_\phi>0,\,U_\phi>0$, so that $\eta=(1/2)\arctan(U_\phi/Q_\phi)$. The total differential is then:

$$\delta \eta = \frac{Q_{\phi} \delta U_{\phi} - U_{\phi} \delta Q_{\phi}}{2(Q_{\phi}^2 + U_{\phi}^2)}.$$
 (7)

We can see that the above expression is on the order of 1/(2(S/N)), where S/N is the signal-to-noise ratio of polarized intensity defined as $\delta PI/PI$, with PI being the polarized intensity. This estimate can be made more accurate if we focus on the deviation from the azimuthal pattern where $Q_{\phi} = PI$, $U_{\phi} = 0$, so that $\delta \eta = \delta U_{\phi}/2Q_{\phi} = 1/(2(S/N))$.

For the 10° angle deviation we obtained before, we need $S/N \leqslant 7.8$. In the survey presented by Avenhaus et al. (2018), the S/N is better than 20 for most cases, which translates into an error in angle of $\delta\eta \sim 1^{\circ}.4$. So if the dust is aligned with the magnetic field in the atmosphere of a moderately inclined disk, we should be able to detect the deviation from the azimuthal polarization pattern as predicted by this work.

5.2. Distinguishing Different Mechanisms

The most important feature of our polarization mechanism is that we relied on elongated dust grains that are aligned with magnetic fields. If a mechanism that produces near-IR scattering polarization accounts for only spherical dust grains or nonspherical dust grains but without grain alignment, the optical properties of the ensemble of dust grains will have spherical symmetry, i.e., the scattering matrix is solely a function of scattering angle. Under this assumption, for light last scattered at the near side (the right point in Figure 5) or at the far side (the left point in Figure 5), the geometry of the scattering problem is symmetric between up and down'. As a result, the end polarization orientation would either be along the radial direction or along the azimuthal direction with no other possible outcomes, which means $U_{\phi} = 0$. In contrast, the U_{ϕ} is maximized near the near-side and far-side points in our models (see, Figure 12).

The main alternative discussed in the literature so far is multiple scattering at high optical depth and high inclination (Canovas et al. 2015). Here we give a heuristic argument on how this mechanism works. If we take single scattering of spherical dust grains as the zeroth order problem, the first-order problem will be the photons scattered twice before they reach our telescope. As discussed above, the zeroth order problem considering only single scattering cannot produce U_{ϕ} . The U_{ϕ} is then produced primarily by the first-order problem with double scattering. Since the disk atmosphere is optically thick at near-IR, the first scattering site cannot be too far from the second scattering site. We shall refer to the particle at the first scattering site as particle A and the particle at the second scattering site as particle B. The light coming from particle B is then what we observe. In this first-order double scattering problem, the local anisotropy of the radiation field as viewed at the location of particle B is what determines the polarization state of the scattered light. If we further ignore the polarization of the light between particle A and B and treat the light scattered by particle A as nonpolarized, the problem reduces to a problem that is the same as the self-scattering problem at high optical depth at (sub)millimeter wavelengths. Particle A is comparable with the original source of the dust thermal emission at (sub)millimeter wavelengths, and particle B is the scattering particle of the self-scattering problem. As discussed by Yang et al. (2017), the polarization orientation is along the "minor axis" of the local disk surface, the direction that is coplanar with both the final scattering direction and the normal direction of the local disk surface (see Figure 1 of Yang et al. (2017) for a schematic illustration and the related texts). With this simple model, we can calculate the U_{ϕ}/I as a function of the azimuthal angle in the disk frame. The results assuming $i = 60^{\circ}$ are shown as the red curves in Figure 14. Note that the absolute values of U_{ϕ}/I from the above simple double scattering model are arbitrary in the sense that the contribution from single scattering is not taken into account in this simple double scattering model. The single scattering does not produce U_{ϕ} , so it should not affect the overall profile, if azimuthal variation in single scattering is ignored. Higher order scattering

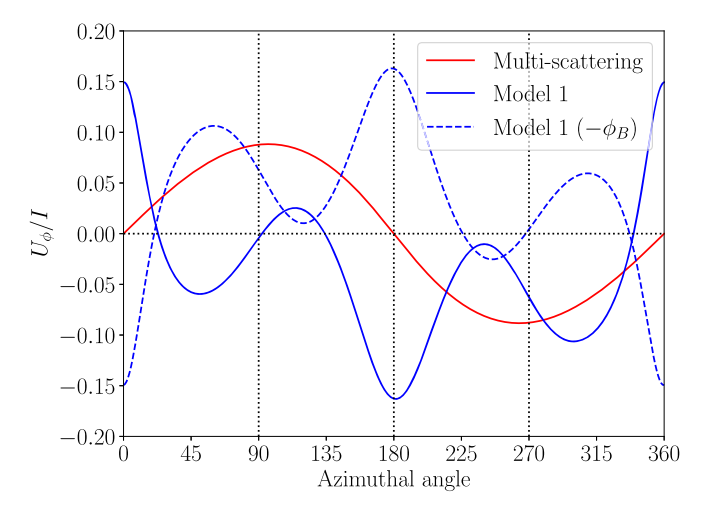


Figure 14. The U_ϕ/I profiles. The red curve shows the U_ϕ/I for multiple scattering, using a simple double-scattering approximation, assuming an inclination angle of 60°. See text for discussions. The blue solid curve comes from the fiducial model, Model 1, with $i=60^\circ$. The blue dashed curve is similar to Model 1, but with $\phi_B=-90^\circ$. This changes the helicity of the assumed magnetic field configurations, but nothing else, resulting in U_ϕ flipping its sign in the whole disk. This is a unique feature for polarization produced by magnetic alignments.

events may have more significant contributions, which are not taken into account here. We choose to multiply the whole curve by 0.2 to make the results comparable with those from the magnetic alignment. Despite the simplicity of this model, it still captures most of the physics and the result agrees with Canovas et al. 2015's moderate opacity model very well. The most important feature of U_{ϕ} generated by multiple scattering is that the U_{ϕ} is opposite between symmetric points with respect to the disk minor axis (0°–180° versus 180°–360°; see Figure 2 of Canovas et al. 2015).

For comparison, we also plot the U_{ϕ} for Model 1 with $i = 60^{\circ}$ as blue curves. We can see that the U_{ϕ} is maximized at the near and far sides, with the near side having a positive 0.15 I and the far side having -0.15 I. If we change the helicity of the magnetic field by changing ϕ_B to $-\phi_B$, the U_{ϕ} at the near and far sides will also flip to their opposite values. The curve for $-\phi_B$ is plotted as a blue dashed curve in Figure 14. We can see that the solid and dashed blue curves are symmetric with respect to the middle point. The U_{ϕ} maps presented in Figure 12 can be changed to the magnetic field configuration with opposite helicity by multiplying the whole map by -1 and then flip upside down. This dependence on the helicity of magnetic fields can be very important in distinguishing our mechanisms from others. If we can infer the helicity of the magnetic fields through the rotation curves in the outflows or jets, we can then check against near-IR scattered polarimetry and see if there are any magnetic field signatures and see if the predicted U_{ϕ} map for the given helicity of magnetic fields agrees with observations.

5.3. Potential Sources with Aligned Grains

Before going into specific systems, we summarize our discussions on the difference between our mechanism that relies on elongated dust grains aligned with magnetic fields and the other mechanisms that rely only on scattering by spherical dust grains. For an axis-symmetric system, alternative mechanisms with only spherical dust grains will have U_{ϕ}

 $[\]overline{}$ We have also assumed axis-symmetric geometry for the protoplanetary disk. If there are any structures in the protoplanetary disk, the local radiation field will not have symmetry between up and down. Mechanisms like multiple scatterings Canovas et al. (2015) that relies on the anisotropy of the local radiation field will also produce a nonzero U_{ϕ} component. We will ignore such cases for now.

map being symmetric with respect to the minor axis of the disk. The symmetry is to be considered in the sense of opposite signs. That is to say, if there is a structure of positive U_{ϕ} in one side of the disk, there has to exist the exact same structure of negative U_{ϕ} in the other side of the disk, with these two structures being mirror symmetric with respect to the minor axis. For our mechanism that relies on elongated dust grains, there is no such requirement, and the U_{ϕ} map can even be dominated by either positive or negative U_{ϕ} (see, Figure 12). The asymmetry in the U_{ϕ} map with respect to the minor axis and/or predominant positive/negative U_{ϕ} in axis-symmetric systems are both signs of our mechanism.

With this in mind, we find that CU Cha, HD 169142, MWC 614, Hen 3-365, and HD 142527 are some good candidates for the Gemini-LIGHTS survey (Rich et al. 2022). They all show clear deviations from mirror symmetry expected for scattering by only spherical dust grains. In addition, the outer disk of HD 142527are predominantly positive. Similarly, HD 169142 is also predominantly positive. HD 34700 A has U_{ϕ} maximized along the minor axis, which cannot be explained by spherical dust grains. MWC 614 has clear asymmetry in U_{ϕ} and is slightly more positive than negative U_{ϕ} . We include Hen 3-365 (HD 87643) as a good candidate, despite its nonaxisymmetric structures, which complicate the interpretation. In addition to the substantial asymmetry in the U_{ϕ} image, Hen 3-365 has a wedge of negative Q_{ϕ} (see also Laws et al. 2020), similar to Model 1 (see, Figure 12). In the DARTTS-S survey (Avenhaus et al. 2018), we find V4046 Sgr and DoAr 44 as candidates based on their asymmetric U_{ϕ} images.

We would like to note that the calibration of near-IR polarimetry data is a very complicated process. Part of the calibration involves correction for instrumental polarization, stellar polarization, and/or foreground interstellar contamination. Since there is no priori knowledge of what the stellar polarization and interstellar polarization are, a parameterized approach is usually adopted (Avenhaus et al. 2018). How these effects affect the detection of the signals predicted in this work remains to be determined.

6. Summary

In this paper, we have studied the scattering of the near-IR stellar light by small dust grains, that are aligned with respect to the magnetic fields, in the atmosphere of a protoplanetary disk. We focused on the polarization orientation of the scattered light and showed that the deviation from the often assumed azimuthal pattern can be significant. The main findings are as follows.

- 1. We calculated the polarization pattern in a disk frame (DF). We focused on two models: Model 1 with a relatively large inclination angle ($i = 60^{\circ}$) and a large toroidal magnetic field component and Model 2 with moderate parameters ($i = 45^{\circ}$). Model 1 has polarization reversal, i.e., the scattered light is polarized in the radial rather than azimuthal direction, at certain locations. Model 2 does not have polarization reversal, but still has a maximum angle difference of 11° , detectable if we have S/N > 7.8 for Stokes parameters.
- 2. We gave a geometric explanation of the polarization reversal in Section 3.2. We showed that the polarization reversal is almost inevitable for disks with large

- inclination angles $i > 75^{\circ}$, regardless of the magnetic field configuration.
- 3. The angle difference strongly depends on the field configuration. In particular, it increases with an increasing toroidal component of the magnetic field. Hence it can be used to probe the launching mechanism of magnetized disk wind.
- 4. With a simple minimum mass solar nebular model, we studied the $\tau = 1$ surface for scattering near-IR stellar light and found that the maximum grain size there is on the order of $1 \mu m$, assuming a turbulent viscosity of $\alpha = 10^{-4}$. This justifies the focus of this initial study on relatively small grains.
- 5. We calculated synthetic U_{ϕ}/I and Q_{ϕ}/I maps for the two disk models on the $\tau=1$ surface. The peak U_{ϕ}/I is on the order of \sim 0.15 and \sim 0.05 for Models 1 and 2, respectively. Interestingly, the U_{ϕ}/I is reversed with magnitude unaffected if we change the azimuthal direction of the magnetic field (through $\phi_B \rightarrow -\phi_B$). This effect, together with disk rotation information, can be used to distinguish our mechanism from other U_{ϕ} -producing mechanisms.
- 6. We conducted a grain alignment analysis at the $\tau = 1$ surface. We found that radiative alignment torque should be operating. For regular paramagnetic dust grains, our model favors k-RAT, i.e., grains aligned with radial stellar light. If grains possess substantial superparamagnetic inclusions, B-RAT becomes likely.
- 7. We compared the azimuthal profiles of U_{ϕ} between our model and an alternative model that relies on multiple scattering of spherical dust grains. We argue that a spatial distribution of U_{ϕ} that is predominantly positive or negative and/or asymmetric respective to the minor axis of an intrinsically axisymmetric disk are signals of aligned elongated dust grains. We identified a handful of systems in the existing literature that are potential targets to look for magnetically aligned grains in future studies.

We thank the referee for a detailed and constructive report that helped improve our manuscript significantly. The authors thank Gregory J. Herczeg and Ruobing Dong for comments and suggestions that helped to improve the manuscript. Z.Y.L. is supported in part by NASA 80NSSC20K0533 and NSF AST-1815784.

Appendix A Angle Difference in Grain Frame

In this appendix, we expand on the discussion of the scattering-induced polarization in the grain frame presented in Section 2.

The geometry of the setup is shown in Figure A1. The scattering particle is placed at the center of the frame, with z direction along the symmetry axis of the grain. The blue arrow denotes the incoming light \hat{n}_i , which is placed in the xz plane, without loss of generality. It makes an angle i with the z-axis. The red arrow denotes the scattered light \hat{n}_s , defined by two position angles, θ and ϕ . For the incoming light, its polarization is defined with \hat{e}_1 and \hat{e}_2 . A positive Q corresponds to polarization along \hat{e}_1 and a positive Q corresponds to polarization along a direction bisecting \hat{e}_1 and \hat{e}_2 . For the scattered light, its polarization is defined with $\hat{\theta}$ and $\hat{\phi}$. Here, a positive Q corresponds to polarization along $\hat{\theta}$ and a positive Q

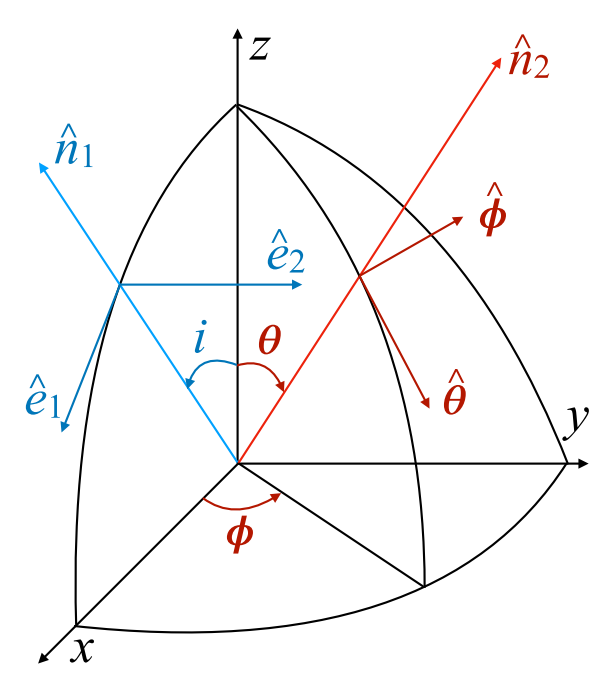


Figure A1. The geometry of our setup in the grain frame. The dust grain is located at the origin. The incoming light is propagating along \hat{n}_1 , making an angle i with z-axis in xz plane, with \hat{e}_1 and \hat{e}_2 as the base vectors for polarization decomposition. The scattered light is propagating along \hat{n}_2 with directional angles (θ, ϕ) . The base vectors for polarization decomposition are $\hat{\theta}$ and $\hat{\phi}$. See text for more details.

corresponds to polarization along a direction bisecting $\hat{\theta}$ and $\hat{\phi}$. The polarization orientation angle η is defined in the $\hat{\theta}$ - $\hat{\phi}$ plane as the angle starting from $\hat{\theta}$ and increasing toward $\hat{\phi}$ counterclockwise, with values between 0° and 180° .

In Appendices A.1–A.5, we will limit our discussions to the dipole approximation (for small grains) to gain a better understanding. The calculation is done with the electrostatic approximation or dipole approximation (Bohren & Huffman 1983). See Appendix B for a brief description of this method. The impact of large dust grains is briefly discussed in Appendix A.6.

A.1. Scattering by Small Spherical Particles

Before calculating the polarization from scattering off elongated dust grains, let us first look at the simpler case for spherical particles when $i=45^\circ$. In the left two panels of Figure A2, we show the polarization fraction p (first left; defined as $\sqrt{Q^2+U^2}/I$) and the polarization orientation angle η (second left) as we change the direction of the scattered light. Note that since the particle is perfectly spherical, the polarization is completely determined by the angle between \hat{n}_i and \hat{n}_s and the results contain no new information but the well-known polarization profile $p=\sin^2<\hat{n}_i,\,\hat{n}_s>/(1+\cos^2<\hat{n}_i,\,\hat{n}_s>)$ and the fact that the polarization direction is perpendicular to both \hat{n}_i and \hat{n}_s . Nonetheless, the spherical case in the left two panels of Figure A2 will serve as a benchmark to help us understand the cases for aspherical dust grains later.

In the first left panel of Figure A2, we overlay a curve that has p = 1, i.e., the scattered light is fully polarized. In this small spherical dust grain case, this is the direction that is perpendicular to the incoming light direction.

In the second left panel of Figure A2, we can clearly see that there exist two singular points, one with $(\theta=45^{\circ}, \phi=0^{\circ})$, and one with $(\theta=135^{\circ}, \phi=180^{\circ})$. These two points correspond to the forward scattering and backward scattering, correspondingly. In these two directions, the polarization fraction in scattered light is 0, and the polarization direction is ill defined. If we walk around the singular point while fixing θ , the polarization will be along $\hat{\theta}$ direction, in order to be perpendicular to both incoming and scattered light. Similarly, if we walk around the singular point while fixing ϕ , the polarization will be along $\hat{\phi}$ direction. Note that $\eta=0^{\circ}$ and $\eta=180^{\circ}$ correspond to the same polarization orientation.

It is worth mentioning that the polarizability matrix (see Appendix B and Equation (B4)) in this spherical case is isotropic and diagonal: $\bar{\alpha} = \text{diag}\{\alpha_s, \alpha_s, \alpha_s\}$, where

$$\alpha_s = a^3 \frac{\epsilon - 1}{\epsilon + 2},\tag{A1}$$

with a being the grain size, and ϵ is the complex dielectric function.

A.2. Fiducial Case

Now let us move on to the more interesting case with aspherical dust grains. For our fiducial case, we consider a small dust grain in the dipole regime. In this work, we consider only oblate dust grains characterized by an aspect ratio s > 1, which we set to s = 1.5 in our fiducial case. In the grain frame depicted in Figure A1, the symmetry axis of the dust grain is placed along the z direction. The light makes an angle $i = 45^{\circ}$ with the z direction, the same as the spherical case discussed above. For the fiducial model and most of the models in this paper, we assume the composition from Birnstiel et al. (2018). It is a mixture of 20% water ice (Warren & Brandt 2008), 33% astronomical silicates (Draine 2003), 7% troilite (Henning & Stognienko 1996), and 40% refractory organics (Henning & Stognienko 1996) by mass. Throughout this paper, we assume an observing wavelength of 1.5 μ m. The results are largely independent of the specific choice of wavelength. The results are shown in the right panels of Figure A2.

In the grain frame, the polarizability matrix is always diagonal as $P = \text{diag}\{\alpha_1, \alpha_1, \alpha_3\}$, and $|\alpha_1| > |\alpha_3|$ because we assume oblate dust grains. See Appendix B for more details. For incoming radiation propagating along the \hat{n}_i direction, we can decompose the light into two components: $E_i = E_1\hat{e}_1 + E_2\hat{e}_2$. The dipole excited in response to these two components are:

$$\mathbf{P}_1 = \bar{\alpha} E_1 \hat{e}_1 = \alpha_1 E_1 \hat{x} \cos i - \alpha_3 E_1 \hat{z} \sin i, \tag{A2}$$

and

$$\mathbf{P}_2 = \bar{\alpha} E_2 \hat{e}_2 = \alpha_1 E_2 \hat{\mathbf{y}}. \tag{A3}$$

We can see that P_2 is always along y direction, i.e., the \hat{e}_2 direction. At the same time P_1 is not along the \hat{e}_1 direction any more, due to the difference between α_1 and α_3 . This is the very reason why scattering by aligned aspherical grains is different from scattering by spherical grains.

In the third left panel of Figure A2, we can see that the maximum polarization is still p = 1, i.e., fully polarized. The location where p = 1 is achieved is plotted as a solid curve in the figure. The p = 1 curve for the spherical case is also plotted in the figure as a dashed line. We can see that the p = 1

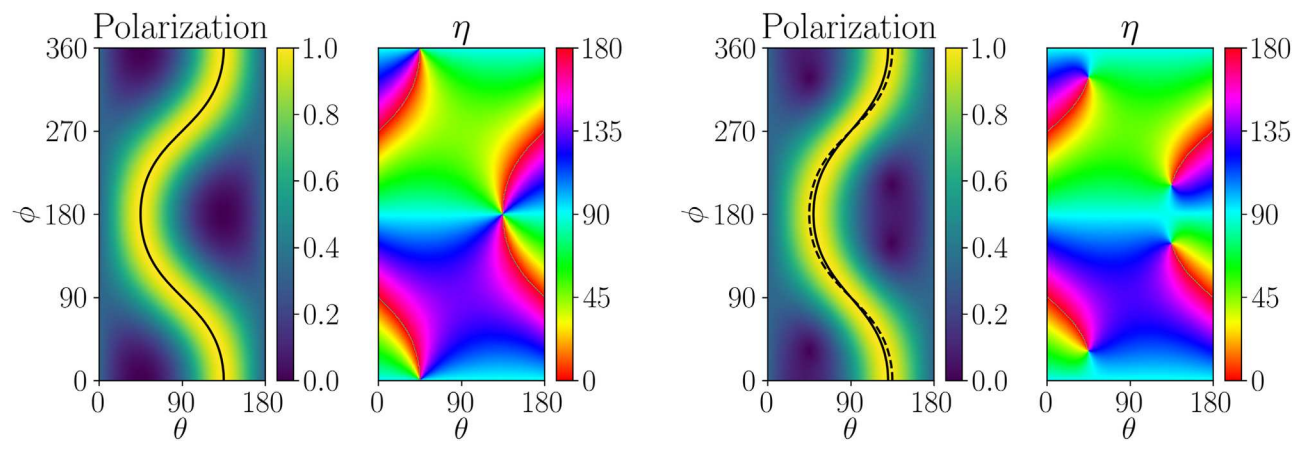


Figure A2. Left two panels: the results for small spherical dust grains. The first left panel shows the polarization fraction for different scattered light direction (θ, ϕ) . The second left panel shows the polarization orientation angle η . $\eta = 0$ means polarization along $\hat{\theta}$. Right: the same, but for results for our fiducial case: a small oblate dust grain with an aspect ratio s = 1.5. The scattering inclination angle is $i = 45^{\circ}$.

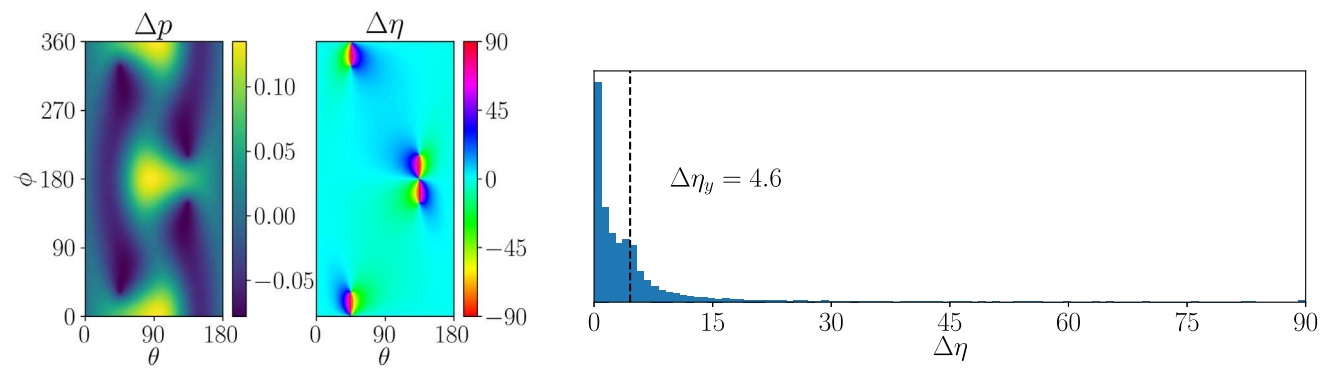


Figure A3. The difference between the spherical and fiducial cases. Left: the difference in polarization fraction. Middle: the difference in polarization orientation. Note that $\Delta \eta = \pm 90^{\circ}$ denote the same polarization state. Right: histogram of angle difference $\Delta \eta$. The angle difference between the dipole P_1 and \hat{e}_1 , i.e., $\Delta \eta_y = 4.7^{\circ}$, is also plotted as a vertical dashed line.

locations are slightly different between these two cases. The difference is zero at $\theta = 90^{\circ}$, $\phi = 90^{\circ}$, or 270° directions. This is because these two directions correspond to the $\pm \hat{y}$ direction, which is along the dipole P_2 . As a result, P_2 does not contribute to the scattered light, and the scattered light is fully polarized.

Along the $\phi=0$ line in the right-most panel of Figure A2, the full polarization (p=1) is achieved at $\theta=130^\circ.3$. It differs from 135° in the spherical case, by 4°.7, due to the difference in direction between P_1 and \hat{e}_1 . This is also the difference in the polarization orientation η (Right panel of Figure A3) at $\theta=90^\circ$ and $\phi=90^\circ$ or 270°, which is for the same reason.

In the right panel of Figure A2, we first notice that the singular points for the spherical grains ($(\theta = 45^{\circ}, \phi = 0^{\circ})$) and $(\theta = 135^{\circ}, \ \phi = 180^{\circ}))$ are no longer singular. There are two reasons for this behavior. First, the forward scattering direction \hat{n}_1 is no longer perpendicular to P_1 . As a result, the emission is no longer maximized for the dipole radiation from P_1 , making it inferior to the radiation from P_2 . Second and more importantly, $|P_1| < |P_2|$ because $\alpha_1 > \alpha_3$. These two reasons combine to make the dipole radiation from P_2 dominate over that from P_1 in the forward and backward scattering directions. At these two singular points in the spherical cases, the polarization is thus along P_2 direction, with $\eta = 90^{\circ}$. Because η near these points can be 0° when varying along constant θ , the difference in polarization orientation between the spherical case and aligned aspherical case is always as large as 90° near these points. There still exist singular points in the diagram for the

aspherical case. They are located symmetrically around the previous singular points with the same θ but different values of ϕ between the spherical and fiducial cases.

In the left two panels of Figure A3, we show the difference in polarization degree and the difference in η for different scattering directions. We can see that the difference in polarization degree can reach up to 13%. The difference in η strongly depends on the scattered light direction. Near the forward and backward scattering direction, i.e., the singular points in the spherical case, $\Delta \eta \approx 90^\circ$, which applies up to the new singular points and forms ribbon-like structures in the $\Delta \eta$ plot.

In the right panel of Figure A3, we show the histogram of the angle difference $\Delta\eta$. We use a vertical dashed line to show $\Delta\eta=4.7^\circ$, which is the angle difference between \hat{e}_1 and P_1 . We can see that while most scattering directions have $\Delta\eta\lesssim4^\circ.7$, a fraction of them have substantially larger $\Delta\eta$ of $10^\circ-20^\circ.$

A.3. Dependence on the Dust Aspect Ratio

To compare the angle difference with different dust models and/or different inclination angles, we propose the following two metrics. The first one is the $\Delta\eta$ at the scattering angle of $\theta=90^\circ$ and $\phi=90^\circ$, which we call $\Delta\eta_y$. This is always the direction along P_2 (and \hat{y}) and hence the scattered light comes purely from P_1 , so that the $\Delta\eta_y$ equals the angle difference between P_1 and \hat{e}_1 .

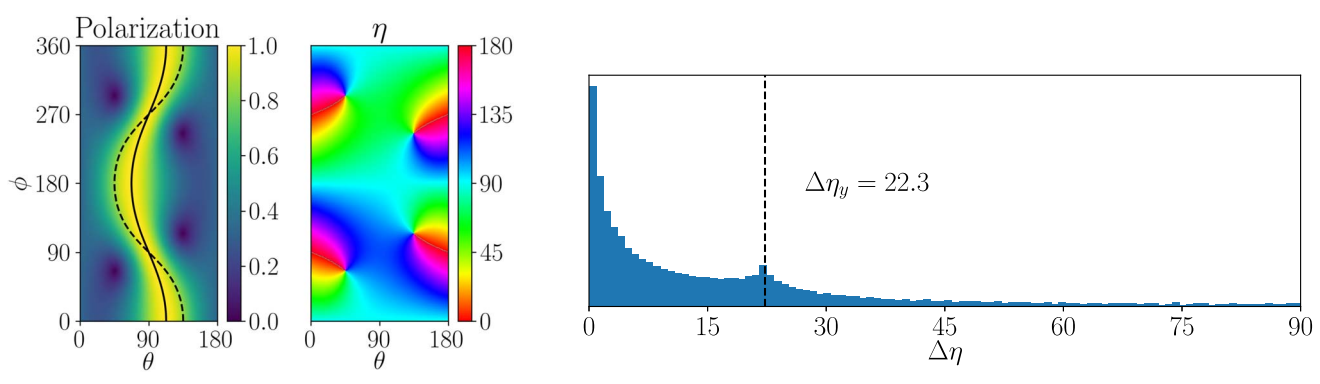


Figure A4. Results for an extremely flattened oblate grain with s = 100. The left two panels are the same as Figure A2. The right panel is the same as the right panel of Figure A3.

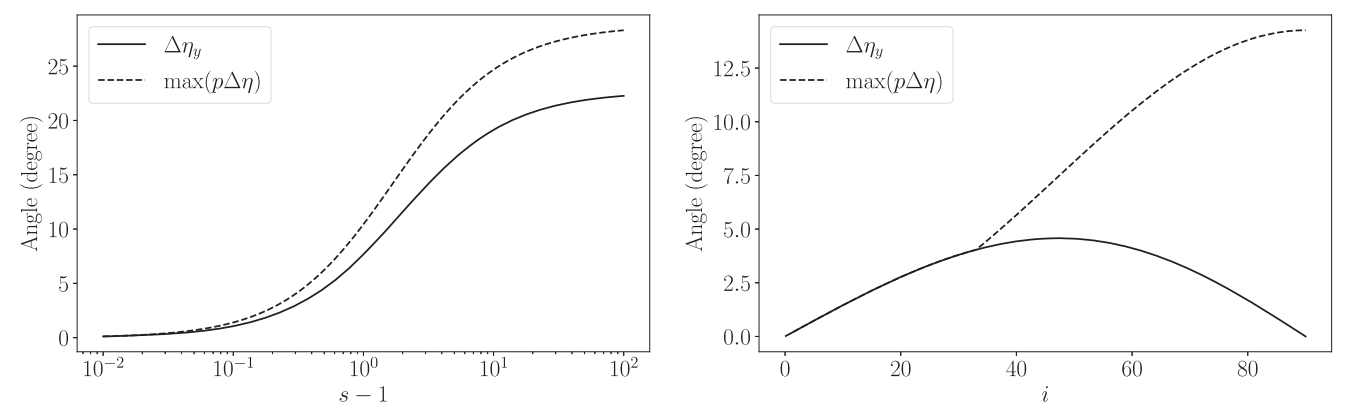


Figure A5. Left: the two metrics of the angle difference as a function of the different dust aspect ratio s. Right: the two metrics for the angle difference as a function of the incoming light inclination angle i for a fixed grain aspect ratio of s = 1.5. See the text for the definitions of the two metrics.

In the upper panels of Figure A4, we show the results for an extreme case with s=100 and its comparison with the spherical case, again assuming $i=45^{\circ}$. We can clearly see in the upper left panel that the p=1 curve moves closer to $\theta=90^{\circ}$ line. This is due to the fact that $|\alpha_1|\gg |\alpha_3|$, so that P_1 is close to \hat{x} . In the limit that $P_1||\hat{x}$, it can be easily verified that only scattered lights in the xy plane, with $\theta=90^{\circ}$, are fully polarized.

In the lower panel of Figure A4, we show the histogram for the s=100 case. The vertical dashed line represents $\Delta \eta_y = 22^{\circ}.3$. We can see that $\Delta \eta_y$ nicely characterizes the angle difference in this case as well, with most scattered light having an angle difference comparable to or less than $\Delta \eta_y$.

While $\Delta\eta_y$ sets a scale for the most probable angle difference, it does not provide a good description for the spread in the histogram beyond $\Delta\eta_y$. To characterize the spread, we propose a second metric $\max(p\Delta\eta)$, the maximum value of $p\Delta\eta$ for all scattering directions. It is motivated by the fact that large $\Delta\eta$ directions tend to have low polarization fractions (see Figure A2 and Figure A4). In the case of s=100, we have $\max(p\Delta\eta)=29^{\circ}7$. Note that we always have $\max(p\Delta\eta)\geqslant \Delta\eta_y$, because when scattered toward \hat{y} , we have p=1 and $\Delta\eta=\Delta\eta_y$. The difference between $\max(p\Delta\eta)$ and $\Delta\eta_y$ is a measure of the spreading beyond $\Delta\eta_y$.

In the left panel of Figure A5, we show the two metrics, $\Delta \eta_y$ and $\max(p\Delta \eta)$, as a function of the aspect ratio s. We can clearly see that more flattened (oblate) grains have larger deviations in polarization orientation due to scattering compared to spherical grains. For s=2, the angle difference

is typically on the order of 10° , while for extremely elongated grains, the difference can be as large as 30° for a large fraction of scattering angles.

A.4. Dependence on the Inclination Angle

In the right panel of Figure A5, we show the two metrics, $\Delta\eta_y$ and $\max(p\Delta\eta)$, as a function of the inclination angle i. We can see that $\Delta\eta_y$ increases as we increase the inclination angle i initially, then falls back to 0 as we go toward $i=90^\circ$. In the two limiting cases, i=0 and $i=90^\circ$, we have $\Delta\eta_y=0$. This is because \hat{e}_1 becomes aligned with one of the principal axes (\hat{z} for i=0 and \hat{x} for $i=90^\circ$), hence $P_1\|\hat{e}_1$. However, this does not imply the angle difference also goes to 0 as the inclination angle approaches 90° . In fact, for larger inclination angles, the difference between $|P_1|$ and $|P_2|$ increases with i, and the polarization orientation deviates from the spherical case (with $|P_1|=|P_2|$) progressively. These differences are not captured by the first metric $\Delta\eta_y$.

At a larger inclination angle, there is a stronger need for the second metric. To see what exactly happens at a larger inclination angle, we show the polarization fraction and angle difference for $i=75^{\circ}$ in the upper panels of Figure A6. To compare, we show the same for $i=15^{\circ}$ in the lower panels of Figure A6. These two models have similar $\Delta\eta_y$ (2°.5 and 2°.1 for $i=75^{\circ}$ and $i=15^{\circ}$, respectively). We can see that even though the deviations of the p=1 locations from corresponding spherical models are similar for these two inclination angles, the ribbon-like structures are much larger in $i=75^{\circ}$ than in $i=15^{\circ}$. This results in a larger spread in the histogram

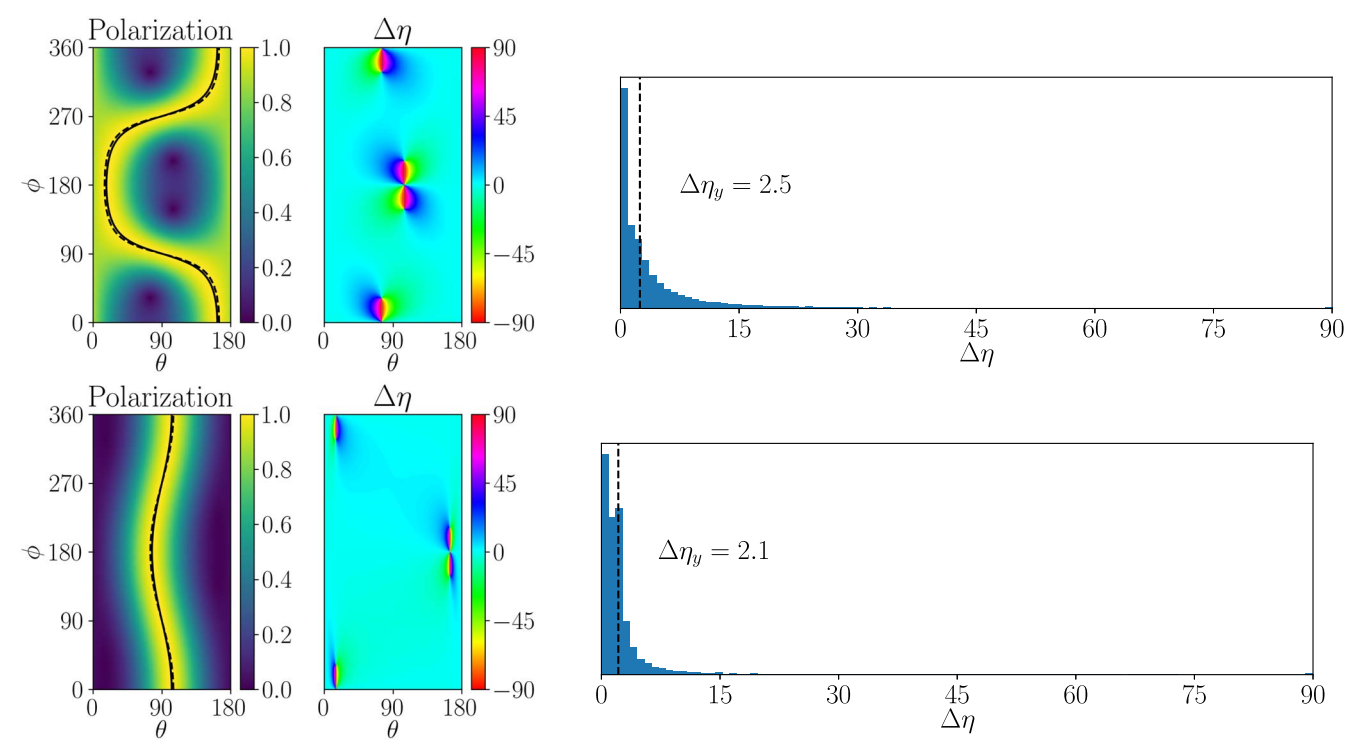


Figure A6. Results for $i = 75^{\circ}$ and $i = 15^{\circ}$. Top panels: results for $i = 75^{\circ}$. From left to right shows the polarization fraction, the angle difference with the spherical case, and the histogram of angle differences. Bottom panels: results for $i = 15^{\circ}$ in the same order.

 Table A1

 Angle Difference for Different Compositions

Composition	n	k	$\Delta \eta_{y}$	$\max(p\Delta\eta)$
DSHARP ^a	1.56	2.0×10^{-2}	4.°6	6.°2
Silicate ^b	1.69	3.2×10^{-2}	5°3	7°3
Troilite ^c	6.57	2.59	12°6	16.°8
Water iced	1.29	4.7×10^{-4}	2°6	3°.5
Organics ^c	1.62	2.0×10^{-2}	4°9	6.°8

Notes. Assuming $i = 45^{\circ}$ and s = 1.5 at an observing wavelength of 1.5 μ m.

of angle differences in $i = 75^{\circ}$ than $i = 15^{\circ}$, shown in the right panels of Figure A6.

This spread is nicely captured by our second metric, $\max(p\Delta\eta)$, which are 13°.2 and 2°.1 at $i=75^\circ$ and $i=15^\circ$, respectively. According to $\max(p\Delta\eta)$, there is a substantial fraction of scattering directions with angle differences as large as $\sim\!13^\circ$ when $i=75^\circ$, even though the $\Delta\eta_v$ is only 2°.5.

With a better understanding of the two metrics, $\Delta \eta_y$ and $\max(p\Delta\eta)$, we now come back to the right panel of Figure A5. We conclude that the angle difference with the spherical model increases monotonically as the inclination angle i increases. There is a large fraction of scattering directions with $\Delta\eta$ of $\sim 15^\circ$ or larger when i is close to 90° .

Interestingly, $\max(p\Delta\eta) = \Delta\eta_y$ for small inclination angles. In these cases, the ribbon-like structures are very thin and the angle difference is dominated by the difference between P_1 and \hat{e}_1 (see upper lower panels of Figure A6).

A.5. Dependence on Dust Composition

The composition of dust has a strong impact on the optical properties of dust grains. To show the dependence of angle difference on dust composition, we calculated $\Delta\eta_y$ and $\max(p\Delta\eta)$ assuming $i=45^\circ$ and s=1.5 for five illustrative dust compositions. The results are tabulated in Table A1. We also listed the real (n) and the imaginary part (k) of the refractive index for each composition at the wavelength $\lambda=1.5~\mu\mathrm{m}$.

Among the materials considered, troilite produces the largest angle difference. This may be related to its absorptive nature, characterized by its large imaginary part of the refractive index k.

A.6. Results for Moderately Large Dust Grains

The size of grains has a strong impact on dust scattering. To relax the previous small grain size assumption, we use the PyTMatrix⁸ module (Leinonen 2014), which is a wrapper for the TMatrix code (Mishchenko & Travis 1994). The results for MRN-distributed dust grains with s=1.5 and $a_{\rm max}=1\mu{\rm m}$, corresponding to a size parameter of $x_{\rm max}=4.2$, are shown in Figure A7. We can see that the polarization fraction decreases significantly from 100% at the peak curve, but the distribution of η is still similar to the one in the dipole regime in the right panels of Figure A2. The histogram of the angle difference is also larger for the $1\mu{\rm m}$ grains. The dipole approximation is reasonable for $1\mu{\rm m}$ grains or smaller if we focus on the polarization orientation η .

We note that even larger grains ($a_{\text{max}} \ge 2 \,\mu\text{m}$) can produce more complicated polarization patterns and distributions of η (results not presented in this paper), which are harder to use for

^a Birnstiel et al. (2018);

^b Draine (2003);

^c Henning & Stognienko (1996);

^d Warren & Brandt (2008).

⁸ Available at https://github.com/jleinonen/pytmatrix/.

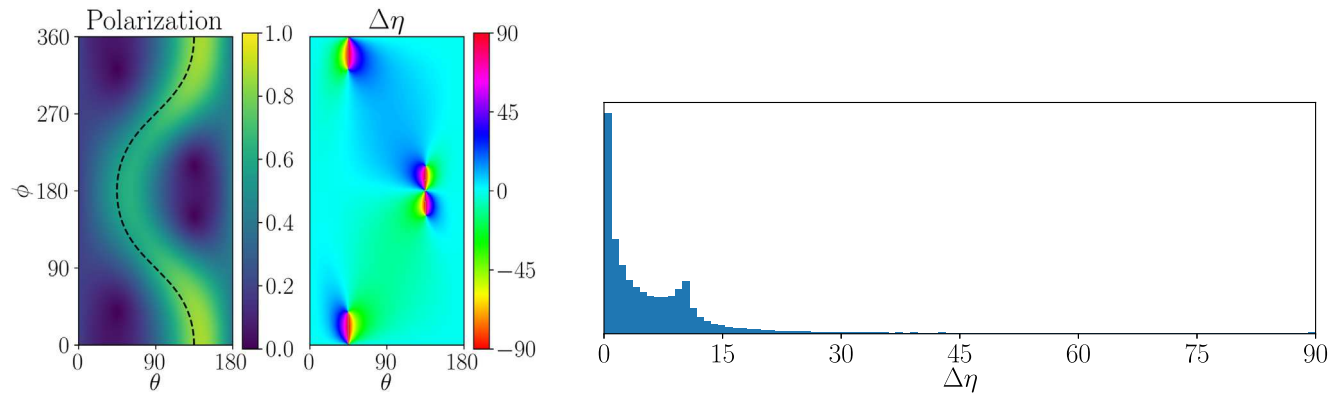


Figure A7. The same as Figure A6 but for MRN-distributed dust grains with $a_{\text{max}} = 1 \mu \text{m}$.

interpreting observational results. Larger grains may account for the strong forward scattering observed in some systems (e.g., Avenhaus et al. 2018). We will postpone a full exploration of larger dust grains to a future investigation and focus on the dipole approximation in this work.

Appendix B Dipole Approximation

Since the dipole approximation is an important part of our methodology, we will describe it briefly together with several key equations to help understand the results in this paper, especially the importance of the quantity $\Delta\eta_y$ defined in Appendix A. In particular, Equation (B3) is the key to calculating the amplitude scattering matrix but is not in the literature as far as we know. For a more detailed derivation and description, we refer interested readers to Bohren & Huffman (1983), especially their Section 5.

When the dust grains are small compared to the observing wavelength, the response of the particle to an external electromagnetic wave can be well represented by a dipole oscillating with the same frequency and phase as the incoming radiation. Let E_i be the E vector of the incoming light. The excited dipole is linear with respect to E_i : $P = \alpha E_i$, where α is the 3×3 polarizability matrix of the dust grain.

The oscillating dipole P will then radiate a secondary electromagnetic wave with an electric field (in far field with $kr \gg 1$):

$$\boldsymbol{E}_{s} = \frac{k^{2}}{r} [(\hat{r} \times \boldsymbol{P}) \times \hat{r}] e^{i(kr - \omega t)}, \tag{B1}$$

where $\hat{r} \equiv r/r$. Decompose the incoming radiation as $E_i = E_{i1}\hat{e}_{i1} + E_{i2}\hat{e}_{i2}$, the scattered radiation as $E_s = E_{s1}\hat{e}_{s1} + E_{s2}\hat{e}_{s2}$, we can define the following amplitude scattering matrix:

$$\begin{pmatrix} E_{s1} \\ E_{s2} \end{pmatrix} = \frac{e^{ik(r-z)}}{-ikr} \begin{pmatrix} S_{11} & S_{12} \\ S_{21} & S_{22} \end{pmatrix} \begin{pmatrix} E_{i1} \\ E_{i2} \end{pmatrix},$$
(B2)

thanks to the far-field dependence of scattered light in Equation (B1). Calculating the dot product of $\hat{e}_{s1} \cdot E_s$ from Equation (B1), we can easily derive the S_{11} and S_{12} . Similarly, we can derive the S_{21} and S_{22} through $\hat{e}_{s2} \cdot E_s$. They can be nicely summarized as follows:

$$S_{mn} = (-ik^3)(\hat{e}_{sm} \cdot \alpha \cdot \hat{e}_{in}), \tag{B3}$$

with m,n = 1,2. Equation (B3) is rotation invariant and can be evaluated in any frame. The dipole approximation is thus free of rotation of Stokes parameters: one can rotate the polarizability matrix into the disk frame once and for all instead of rotating Stokes parameters into the grain frame for every scattering event.

With the amplitude scattering matrix calculated in Equation (B3), the Mueller Matrix relating the incoming and scattering Stokes parameters can be calculated using Equation (3.16) of Bohren & Huffman (1983).

In this work, we use oblate spheroidal particles to represent aligned elongated dust grains. In this case, let $a_1 = a_2 > a_3$ be the three principle semimajor axes and $a^3 = a_1 a_2 a_3$ be the effective radius of the dust grain. We have a diagonal matrix for the polarizability matrix: $\alpha = \text{diag}\{\alpha_1, \alpha_1, \alpha_3\}$, with $|\alpha_1| > |\alpha_3|$. The polarizability is:

$$\alpha_l = a^3 \frac{\epsilon - 1}{3 + 2L_l(\epsilon - 1)},\tag{B4}$$

where ϵ is the complex dielectric function, $L_l(l=1, 2, 3)$ are geometric factors with $L_1 + L_2 + L_3 = 1$. For an oblate spheroid, we have

$$L_1 = \frac{g(e)}{2e^2} \left[\frac{\pi}{2} - \tan^{-1} g(e) \right] - \frac{g^2(e)}{2},$$
 (B5)

where $e^2 = 1 - a_3^2/a_1^2$ is the eccentricity, not to be confused with natural base e in another context. Function $g(e) \equiv \sqrt{(1 - e^2)/e^2}$, and $L_3 = 1 - 2L_1$.

ORCID iDs

Haifeng Yang (杨海峰) ® https://orcid.org/0000-0002-8537-6669

Zhi-Yun Li https://orcid.org/0000-0002-7402-6487

References

Andersson, B.-G., Lazarian, A., & Vaillancourt, J. E. 2015, ARA&A, 53, 501 Avenhaus, H., Quanz, S. P., Garufi, A., et al. 2018, ApJ, 863, 44 Bacciotti, F., Girart, J. M., Padovani, M., et al. 2018, ApJL, 865, L12 Bai, X.-N. 2011, ApJ, 739, 50 Bai, X.-N., Ye, J., Goodman, J., & Yuan, F. 2016, ApJ, 818, 152 Balbus, S. A., & Hawley, J. F. 1991, ApJ, 376, 214 Barnett, S. J. 1915, PhRv, 6, 239

Benisty, M., Juhasz, A., Boccaletti, A., et al. 2015, A&A, 578, L6 Birnstiel, T., Dullemond, C. P., Zhu, Z., et al. 2018, ApJL, 869, L45 Blandford, R. D., & Payne, D. G. 1982, MNRAS, 199, 883

```
Bohren, C. F., & Huffman, D. R. 1983, Absorption and Scattering of Light by
   Small Particles (New York: Wiley)
Canovas, H., Ménard, F., de Boer, J., et al. 2015, A&A, 582, L7
de Boer, J., Langlois, M., van Holstein, R. G., et al. 2020, A&A, 633, A63
Dent, W. R. F., Pinte, C., Cortes, P. C., et al. 2019, MNRAS, 482, L29
Draine, B. T. 2003, ARA&A, 41, 241
Garufi, A., Avenhaus, H., Pérez, S., et al. 2020, A&A, 633, A82
Garufi, A., Dominik, C., Ginski, C., et al. 2022, A&A, 658, A137
Goodman, A. A., & Whittet, D. C. B. 1995, ApJL, 455, L181
Harrison, R. E., Looney, L. W., Stephens, I. W., et al. 2019, ApJL, 877, L2
Hartmann, L., Herczeg, G., & Calvet, N. 2016, ARA&A, 54, 135
Henning, T., & Stognienko, R. 1996, A&A, 311, 291
Hoang, T., & Lazarian, A. 2009, ApJ, 697, 1316
Hull, C. L. H., & Zhang, Q. 2019, FrASS, 6, 3
Hull, C. L. H., Yang, H., Li, Z.-Y., et al. 2018, ApJ, 860, 82
Jones, R. V., & Spitzer 1967, ApJ, 147, 943
Kataoka, A., Tsukagoshi, T., Pohl, A., et al. 2017, ApJL, 844, L5
Laws, A. S. E., Harries, T. J., Setterholm, B. R., et al. 2020, ApJ, 888, 7
```

```
Lazarian, A. 2007, JQSRT, 106, 225
Lazarian, A., & Hoang, T. 2007, MNRAS, 378, 910
Leinonen, J. 2014, OExpr, 22, 1655
Li, D., Pantin, E., Telesco, C. M., et al. 2016, ApJ, 832, 18
Mathis, J. S., Mezger, P. G., & Panagia, N. 1983, A&A, 128, 212
Mathis, J. S., Rumpl, W., Nordsieck, K. H., et al. 1977, ApJ, 217, 425
Mishchenko, M. I., & Travis, L. D. 1994, OptCo, 109, 16
Planck Collaboration, Aghanim, N., Akrami, Y., et al. 2020, A&A, 641, A12
Rich, E. A., Monnier, J. D., Aarnio, A., et al. 2022, arXiv:2206.05815
Stephens, I. W., Yang, H., Li, Z.-Y., et al. 2017, ApJ, 851, 55
Tazaki, R., Lazarian, A., & Nomura, H. 2017, ApJ, 839, 56
Warren, S. G., & Brandt, R. E. 2008, JGRD, 113, D14220
Weidenschilling, S. J. 1977, Ap&SS, 51, 153
Whitney, B. A., & Wolff, M. J. 2002, ApJ, 574, 205
Yang, H. 2021, ApJ, 911, 125
Yang, H., Li, Z.-Y., Looney, L. W., Girart, J. M., & Stephens, I. W. 2017,
   MNRAS, 472, 373
Youdin, A. N., & Lithwick, Y. 2007, Icar, 192, 588
```